

The Impact of Comet Shoemaker-Levy 9 Sends Ripples Through the Rings of Jupiter

Mark R. Showalter^{1,*}, Matthew M. Hedman² and Joseph A. Burns²

¹SETI Institute, 189 Bernardo Avenue, Mountain View, CA 94043

²Cornell University, Ithaca NY 14853

*To whom correspondence should be addressed, e-mail mshowalter@seti.org

Abstract. Jupiter's ring shows vertical corrugations reminiscent of those recently detected in the rings of Saturn. The Galileo spacecraft imaged a pair of superimposed ripple patterns in 1996 and again in 2000. These patterns behave as two independent spirals, each winding up at a rate defined by Jupiter's gravity field. The dominant pattern originated between July and October 1994, when the entire ring was tilted by ~ 2 km. We associate this with the Shoemaker-Levy 9 impacts of July 1994. New Horizons images still show this pattern 13 years later, and suggest that subsequent events may also have tilted the ring. Impacts by comets or their dust streams are regular occurrences in planetary rings, altering them in ways that remain detectable decades later.

On November 9, 1996, the Galileo spacecraft imaged a systematic, unexplained pattern of brightness variations in Jupiter's main ring, suggesting vertical ripples in the ring's surface (1). More recently, Cassini images have revealed a similar pattern in Saturn's rings. That pattern arose from an initially inclined ring, which was slowly twisted into a spiral by Saturn's gravity (2,3). A closer analysis of Galileo data now confirms that the patterns in the rings of Jupiter and Saturn obey identical kinematics, except that Jupiter's ring contains two ripple patterns, not one.

Galileo viewed the rings from nearly edge-on, with opening angle $B = 0.48^\circ$ (Fig. 1, Table S1). The intensity I of an optically thin ring is proportional to the amount of material along the line of sight, so it varies as $\sin(B)^{-1}$. For the Jovian ring, optical depth $\tau < 10^{-5}$ (4,5), so this dependence applies. In this limit, the Sun's opening angle plays no role, because every particle is illuminated equally.

A nonzero surface slope modifies the effective local opening angle, naturally leading to variations in I (6):

$$I \propto 1 / \sin(B) [1 - \sin(\theta)/\sin(B) Z'(R, \theta)]. \quad (1)$$

Here $Z(R, \theta)$ describes the local height of the ring above the equatorial plane in polar coordinates (R, θ) . The radial component of the local slope is $Z'(R, \theta) = \partial Z / \partial R$; we neglect the slope's much smaller tangential component (6,7). Longitudes are measured from the ansa line passing through the ring's tip, where a radial vector is perpendicular to the line of sight.

Note that the dependence of I on $\sin(\theta)$ naturally predicts the reversals of contrast observed in the Galileo image. We have applied Eq. 1 to derive the function $Z'(R)$ at $\theta = 0$ (Fig. 1C). Slopes approach 3% or $\sim 1.5^\circ$. However, unlike the pattern in Saturn's rings (2,3), this one is not a pure sinusoid; a Fourier transform shows two distinct peaks (Fig. 2A). In a least-squares modeling of $Z'(R)$, two sinusoids successfully account for the location of nearly every peak and trough. Matches to the amplitudes are imperfect, however, suggesting that the ring slope may be modulated by other factors that we have not yet considered. The dominant pattern has a wavelength $\lambda_{\text{long}} = 1920 \pm 150$ km and a vertical amplitude $Z_{\text{long}} = 2.4 \pm 0.7$ km; the shorter-wavelength pattern has $\lambda_{\text{short}} = 630 \pm 20$ km and $Z_{\text{short}} = 0.6 \pm 0.2$ km.

If these sinusoidally varying slopes are analogous to the corrugations observed at Saturn (2,3), then they arose from an initially tilted ring that slowly twisted into a spiral pattern due to differential nodal regression. The wavelength of these patterns depends only on the local gravitational field and the amount of time T that has elapsed since the ring became tilted (2,3). Near the middle of the main Jovian ring, the predicted wavelength is

$$\lambda = \sim 4200 \text{ km} / (T/\text{years}). \quad (2)$$

The numerical factor is derived from Jupiter's gravitational harmonics (8). It varies by $\sim 15\%$ within the radial limits considered but, for practical purposes, can be treated as a constant when modeling individual profiles (6).

Compared to Saturn's ~ 30 -km periodicity, the longer wavelengths at Jupiter would imply much younger features. For the long-wavelength pattern, $T = 800 \pm 60$ days, indicating that a ring-tilting event occurred between July 1 and November 1, 1994. The shorter wavelength corresponds to $T = 2430 \pm 80$ days, meaning that the feature originated between early January and early June, 1990; the midpoint is March 19.

Two Galileo images from June 21, 2000 confirm that this pattern is evolving in the predicted manner. The images individually have very poor signal-to-noise properties, and charged particle impacts into the camera's CCD corrupt many pixels (Fig. S1). Nevertheless, combined

processing of both images has enabled us to identify and eliminate most of the corrupted pixels (Fig. 3A). Contrast reversals show up clearly after processing (Fig. 3B), from which we have derived $Z'(R)$ (Fig. 3C). Fourier processing once more identifies two dominant peaks, but now they are at shorter wavelengths (Fig. 2B). Modeling of the ring profile as a superposition of two sinusoids provides a very good description of the data (Fig. 3C, dashed line), with $\lambda_{\text{long}} = 695 \pm 55$ km; $Z_{\text{long}} = 1.8 \pm 0.4$ km; $\lambda_{\text{short}} = 414 \pm 20$ km; $Z_{\text{short}} = 0.6 \pm 0.2$ km. For comparison, if we use Eq. 2 to extrapolate the patterns seen in 1996 forward over the intervening 1289 days, we would expect $\lambda_{\text{long}} = 734$ km and $\lambda_{\text{short}} = 412$ km. Thus, the wavelengths and amplitudes seen in 2000 are consistent with the expected rate of winding of these spiral features.

To complete our data analysis, we examined four images taken just before New Horizons crossed the Jovian ring plane on March 1, 2007 (Figs. S2–S4). Fourier analysis reveals the continuing effects of SL9’s impact (Fig. 2C). Although Z_{long} has diminished to ~ 350 km, this detection attests to the features’ longevity. The shorter pattern can no longer be detected. However, two suggestive new patterns appear, with $\lambda \approx 1315$ km and 775 km (Fig. S4C). If confirmed by later detections, these would indicate that the rings received additional km-scale tilts around September 2001 and December 2003.

A suitable explanation for ring-tilting events must satisfy some very specific requirements. First, each event must occur within a very brief time span (2,3). The nodal regression rate for orbits in the main Jovian ring is $8.5^\circ/\text{day}$, enough to smear out the effects of any event lasting more than a few weeks. Second, these events must be infrequent, with 2–4 occurrences between ~ 1985 and ~ 2006 . Within this context, it is natural to associate the long pattern with the SL9 impacts of July 16–20, 1994. They occurred within the identified window spanning July–October. Although SL9 was earlier regarded as a “once a century” impact, the observed collision of another object into Jupiter on July 19, 2009 suggests that such events may be 5–10 times more frequent than previously thought (9). The chance of one occurring at random within the identified four-month window is 1–3%.

The triggering event for the secondary pattern in Galileo images is less clear. SL9 fractured during its prior perijove on July 7, 1992. It crossed the equator at $R \sim 115,000$ km (10), apparently producing no measurable effect on the ring less than 15,000 km further out. The perijove before that was in mid-1990, within the window defined by the short wavelength and raising the possibility that SL9 triggered this pattern as well. However, backward integrations of

SL9's trajectory place this perijove much further from Jupiter (10,11). Such integrations have large uncertainties, arising from the chaotic nature of SL9's orbit, and because we do not know where to position the center of SL9's mass prior to its breakup (10,11). Thus, we cannot rule out the possibility that SL9 triggered the 1990 pattern, although it must have passed much closer to the ring than it did in 1992. Alternatively, the secondary pattern may have been triggered by a different, unseen comet; this hypothesis is generally compatible with more recent, higher estimates for the frequency of impacts (9). History records other very close passages of Jupiter by comets 16P/Brooks 2 in 1886 and P/Gehrels 3 in 1970 (12).

What mechanism might have enabled SL9 to alter the Jovian ring so dramatically? In 1994, SL9's solid fragments entered Jupiter at southern latitudes on a north-bound trajectory; they never reached the ring plane. However, dust grains associated with SL9's fragments could have been deflected past the planet and into the ring by solar radiation pressure (Fig. 4) (6). Others have explored the effects of radiation pressure on SL9's dust (13,14), but not with an eye toward the consequences for the ring system. We define β as the ratio of radiation pressure to solar gravity (15). Integrations show that grains with $\beta = 0.007$ (radius $\approx 50 \mu\text{m}$), if released at the time of the 1992 perijove and breakup, would be deflected directly into the main ring in 1994 (6). Larger grains can never intercept the ring but smaller ones, if released later, can. The fragments were emitting dust continuously between the 1992 breakup and the 1994 impact (14,16), providing a continuous source of potential ring impactors. Regardless of their ejection date, integrations show that all particles crossing the main Jovian ring do so within the same $\sim 10^\circ$ sector of inertial longitude and within a time span of a few days (6); thus, they naturally satisfy the requirement to offset the ring quickly and systematically.

Because Jupiter's ring is optically thin, every ring constituent responds independently to the influx of cometary dust. To tilt an orbit by 2 km requires that, on average, particles intercept $\sim 10^{-6}$ of their own mass (6). For a ring of 1-cm particles spanning the orbits of Metis and Adrastea (128,000–129,000 km), an integrated fluence of $\sim 10^{-6} \text{ g/cm}^2$ would be required, or $\sim 10^{13} \text{ g}$ in total. Our simulations indicate that 0.2–0.5% of SL9's ejecta smaller than $50 \mu\text{m}$ will intercept this ring (6). We therefore require SL9 to produce $\sim 2\text{--}5 \times 10^{15} \text{ g}$ of dust, amounting to a volume $\sim 2\text{--}5 \text{ km}^3$. For comparison, estimates of the initial diameter of the intact comet range from $D \sim 1.5 \text{ km}$ (17) to 10 km (18). Corresponding volume estimates are $V = 2\text{--}500 \text{ km}^3$. A meta-study (19) concludes $D = 3.5 \text{ km}$ ($V \approx 20 \text{ km}^3$). The fragments of SL9 underwent substantial collisional

evolution shortly after the breakup (13); this can lead to a steep size distribution in which a substantial fraction of the mass is concentrated in the smallest particles. If so, then the larger estimates for SL9’s volume are compatible with our requirements. Our results are difficult to reconcile with the smallest size estimates, which are based on dynamical models of how a loosely-bound rubble pile would break apart (17).

For a given fluence of cometary dust, larger ring bodies are deflected to smaller tilt angles in inverse proportion to their radii. We chose 1 cm for the above calculation because cm-sized particles are likely to achieve the largest tilts; smaller particles can be shattered by the 50- μm impactors (6). Thus, our mass estimate is only valid if the size distribution is steep, so that the ring’s appearance is dominated by the smallest surviving particles (and their ejecta). The Jovian ring’s dust population does steepen markedly above $\sim 30 \mu\text{m}$ (5), suggesting that this assumption is plausible.

The kinematics of these spirals requires that the wavelength be nearly uniform at any given time, but the tilts need not be. In an optically thin ring, they will vary depending on the local ring particle sizes. In Fig. 1C, the inward decrease of the slopes may simply indicate a decreasing population of the cm-sized particles. This is consistent with ring photometry that indicates a rapidly decreasing number of embedded macroscopic bodies interior to the orbit of Metis (20,21).

We now recognize that impacts by comets and/or their dust clouds are common occurrences in planetary rings. On at least three occasions over the last few decades, these collisions have carried sufficient momentum to tilt a ring of Jupiter or Saturn off its axis by an observable distance. Once such a tilt is established, it can persist for decades, with the passage of time recorded in its ever-tightening spiral. Within these subtle patterns, planetary rings chronicle their own battered histories.

Figure Captions

Fig. 1.

(A) Galileo image C0368974139 from November 9, 1996 shows the Jovian ring’s tip. Indicated are the directions in which longitude θ and radius R are measured. (B) We expanded the image vertically, co-added two similar frames for improved signal-to-noise, and subtracted a duplicate

of the image after reversing it top-to-bottom. Most of the image nearly cancels itself out, but the signals of the ripples are reinforced. Neutral gray corresponds to zero; darker areas are negative. (C) A derived profile of the ring's surface slope vs. radius (solid line). For comparison, the dashed line shows a fit involving superimposed patterns triggered on July 19, 1994 and March 19, 1990. In this fit, we have neglected the expected variation in λ with R (6). Note that panels (A–C) have been aligned vertically to employ the same radial/horizontal scale.

Fig. 2.

Fourier transforms of each radial profile of the ring's surface slope, $Z'(R)$. Data are from Galileo in 1996 (A) and 2000 (B), and from New Horizons in 2007 (C). Vertical lines mark the expected wavenumber ($1/\lambda$) for features triggered on July 19, 1994 (dashed) and on March 19, 1990 (dotted). On the vertical axes, the Fourier amplitude values roughly indicate the height of a single sinusoid, of fixed wavelength but variable phase, that best fits the profile.

Fig. 3.

(A) Two Galileo images from 2000 have been overlaid and combined to produce a clear image of the ring's ansa (6). (B) After flipping the image vertically and subtracting, enhancement reveals the pattern of contrast reversals indicating vertical undulations. (C) A derived radial profile of the ring's slope (solid line). For comparison, the dashed line is a best fit using two sinusoidal patterns, with wavelengths defined by our assumed trigger dates of July 19, 1994 and March 19, 1990. The three panels have been aligned to employ the same radial scale; note that this scale is much smaller than that in Fig. 1.

Fig. 4.

The influence of solar radiation pressure on the motion of SL9's fragments is shown as a function of β . Integrations assume that the pieces separated at low relative velocity during the 1992 perijove. The heavy arrow ($\beta = 0$) shows the path of the large, observed fragments. The trajectories of smaller particles are displaced leftward in the diagram; corresponding β values are labeled around the periphery. Particles with $\beta \approx 0.007$ (heavy dashed line) impact the main ring.

References and Notes

1. M. Ockert-Bell *et al.*, The structure of Jupiter's ring system as revealed by the Galileo imaging experiment, *Icarus* **138**, 188–213 (1999).
2. M. M. Hedman *et al.*, Saturn's dynamic D ring, *Icarus* **188**, 89–107 (2007).
3. M. M. Hedman, J. A. Burns, M. W. Evans, M. S. Tiscareno, C. C. Porco, Saturn's curiously corrugated C ring, *Science*, this issue (2011).
4. M. R. Showalter, J. A. Burns, J. N. Cuzzi, J. B. Pollack, Jupiter's ring system: New results on structure and particle properties, *Icarus* **69**, 458–498 (1987).
5. S. M. Brooks, L. W. Esposito, M. R. Showalter, H. B. Throop, The size distribution in Jupiter's main ring from Galileo imaging and spectroscopy, *Icarus* **170**, 35–57 (2004).
6. Information on materials, methods and models is available on Science Online.
7. This formula is only valid where both $\sin(B)$ and $\sin(\theta)/\sin(B) Z'(R,\theta)$ are $\ll 1$; these constraints are satisfied throughout our analysis.
8. R. A. Jacobson, The gravity field of the Jovian system and the orbits of the regular Jovian satellites, *Bull. Amer. Astron. Soc.* **33**, 1039 (2001).
9. A. Sánchez-Lavega *et al.*, The impact of a large object on Jupiter in 2009 July, *Astrophys. J.* **715**, L155–L159 (2010).
10. L. A. Benner, W. B. McKinnon, On the orbital evolution and origin of comet Shoemaker-Levy 9, *Icarus* **118**, 155–168 (1995).
11. P. W. Chodas, D. K. Yeomans, The orbital motion and impact circumstances of comet Shoemaker-Levy 9, in *The Collision of Comet Shoemaker-Levy 9 and Jupiter*, K. S. Noll, H. A. Weaver, P. D. Feldman, Eds. (Cambridge Univ. Press, 1996), pp. 1–30.
12. K. Zahnle, L. Dones, H. F. Levison, Cratering rates on the Galilean satellites, *Icarus* **136**, 202–222 (1998).
13. Z. Sekanina, P. W. Chodas, D. W. Yeomans, Tidal disruption and the appearance of periodic comet Shoemaker-Levy 9, *Astrophys. J.* **289**, 607–636 (1994).
14. J. M. Hahn, T. W. Rettig, Comet Shoemaker-Levy 9 dust size and velocity distributions, *Icarus* **146**, 501–513 (2000).
15. J. A. Burns, P. L. Lamy, S. Soter, Radiation forces on small particles in the Solar System, *Icarus* **40**, 1–48 (1979).
16. H. A. Weaver *et al.*, Hubble Space Telescope observations of comet P/Shoemaker-Levy 9 (1993e), *Science* **263**, 787–791 (1994).

17. E. Asphaug, W. Benz, Size, density, and structure of comet Shoemaker-Levy 9 inferred from the physics of tidal breakup, *Icarus* **121**, 225–248 (1996).
18. Z. Sekanina, P. W. Chodas, D. K. Yeomans, Secondary fragmentation of comet Shoemaker-Levy 9 and the ramifications for the progenitor’s breakup in July 1992, *Plan. Space Sci.* **46**, 21–45 (1998).
19. M. Zamarashkina, Y. Medvedev, Dynamics of comet Shoemaker-Levy 9, *Proc. of ACM* **500**, 457–460 (2002).
20. J. A. Burns, D. P. Simonelli, M. R. Showalter, D. P. Hamilton, C. C. Porco, H. Throop, L. W. Esposito, Jupiter’s Ring-Moon System, in *Jupiter: The Planet, Satellites and Magnetosphere*, F. Bagenal, Eds. (Cambridge Univ. Press, 2004), pp. 241–262.
21. M. R. Showalter *et al.*, Clump detections and limits on moons in Jupiter’s ring system, *Science* **318**, 232–234 (2007).
22. W. Benz, E. Asphaug, Catastrophic disruptions revisited, *Icarus* **142**, 5–20 (1999).
23. E. Grün, G. E. Morfill, G. Schwehm, T. V. Johnson, A model of the origin of the Jovian ring, *Icarus* **44**, 326–338 (1980).
24. MRS acknowledges the support of NASA’s Jupiter Data Analysis Program through grant NNX09AD97G. JAB has been funded by NASA’s Planetary Geology and Geophysics Program.

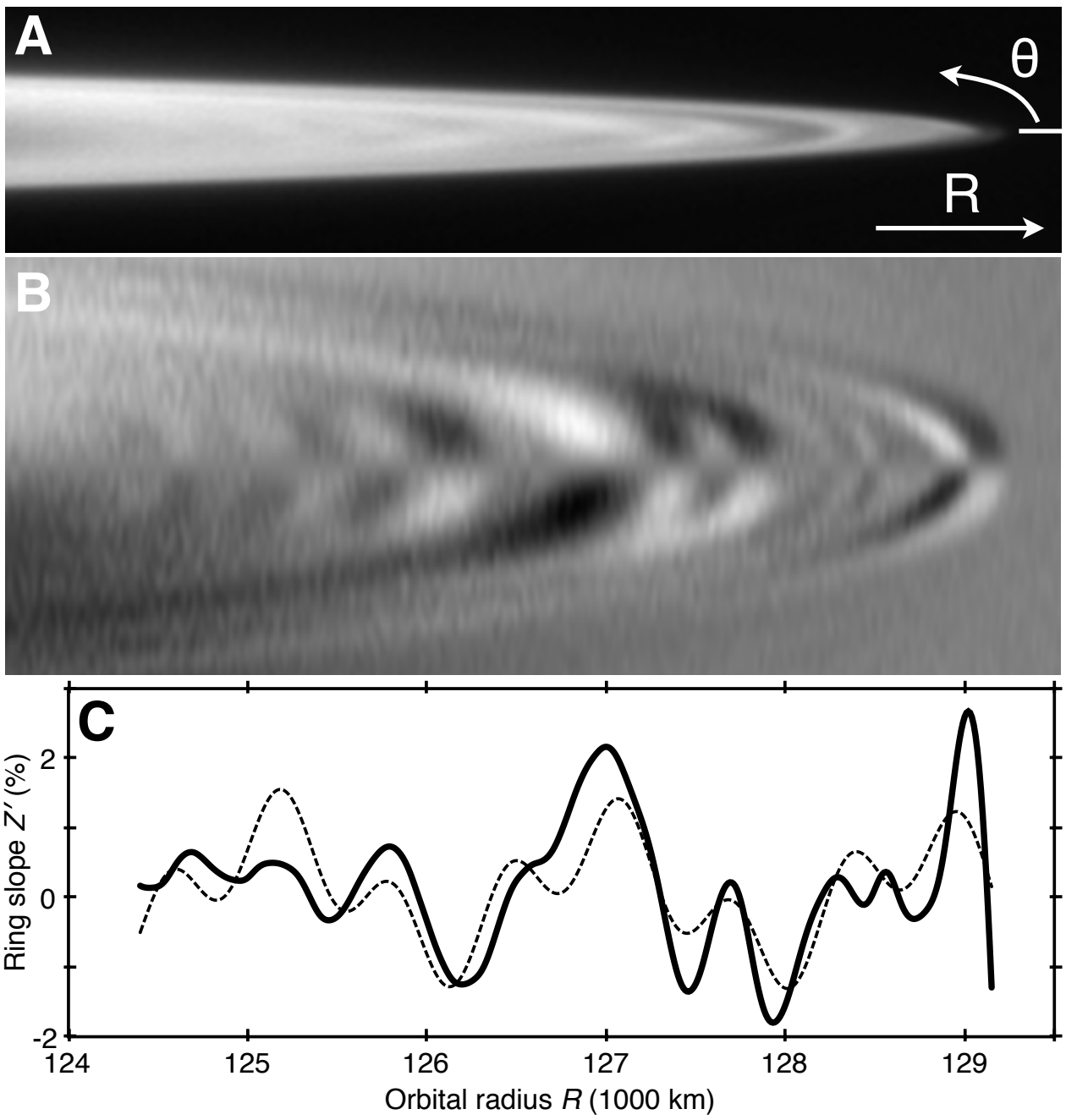
Supporting Online Material

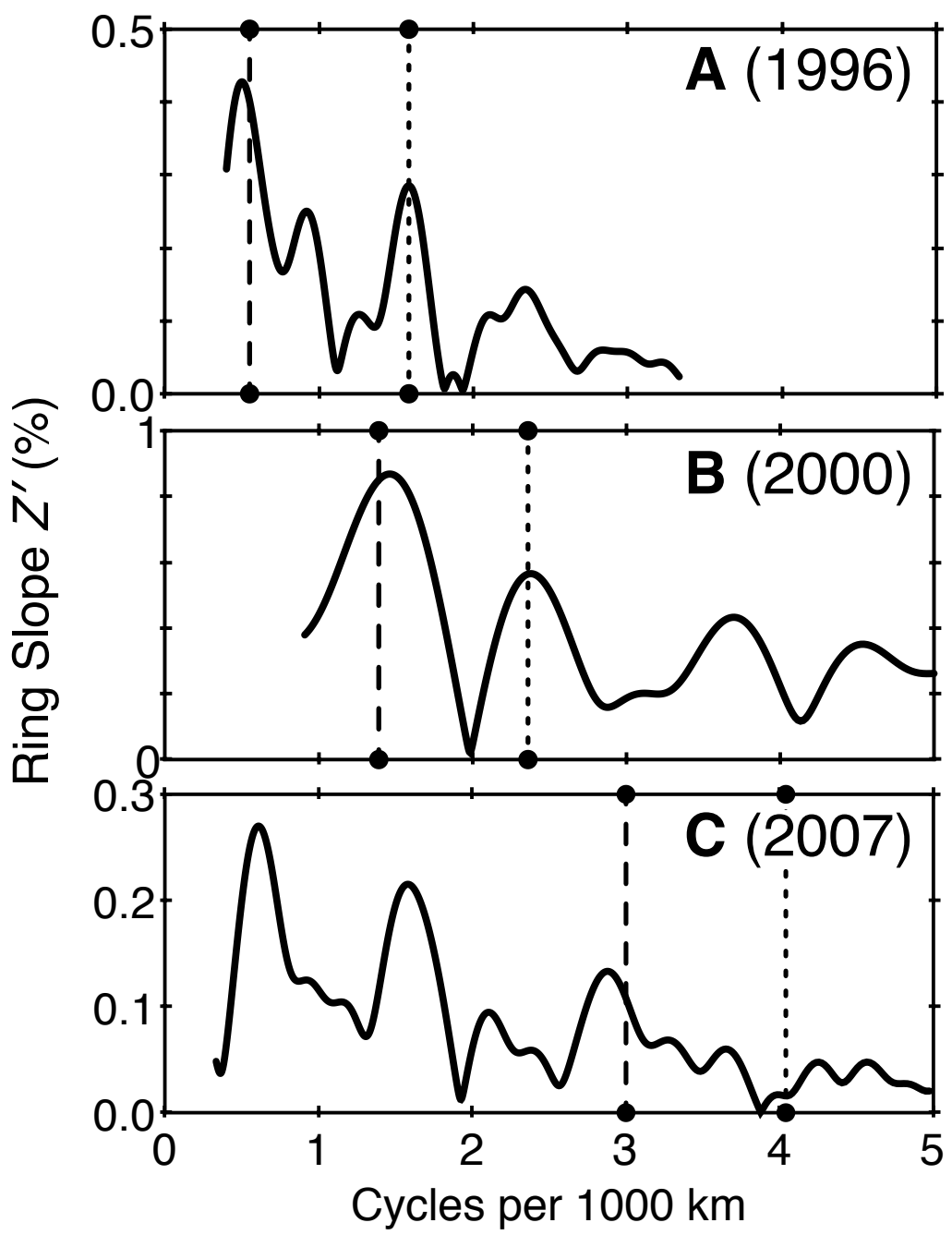
www.sciencemag.org

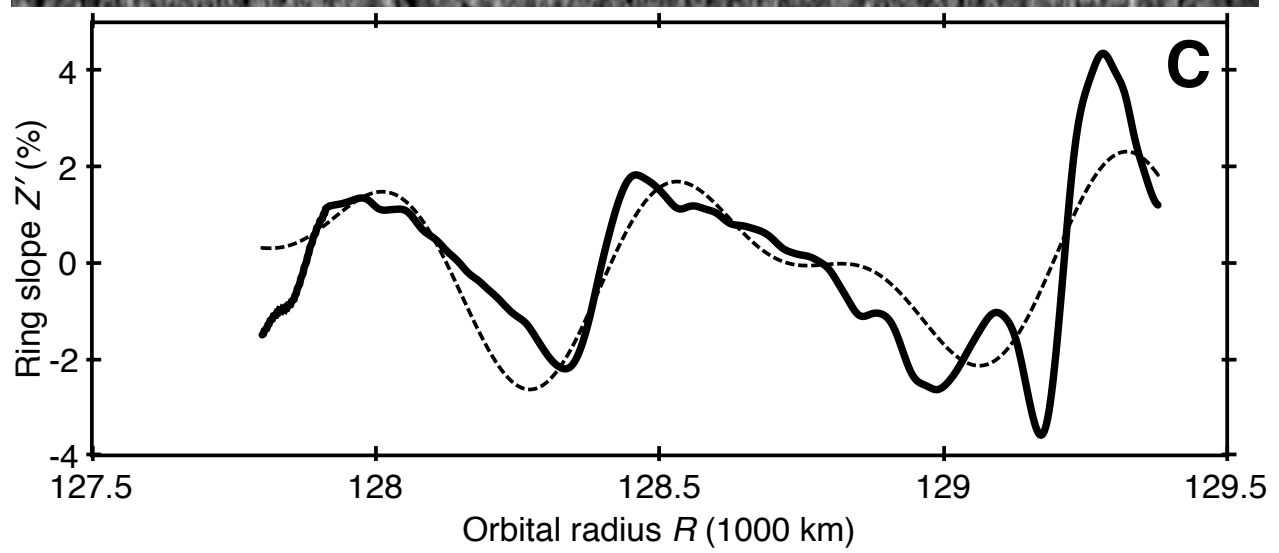
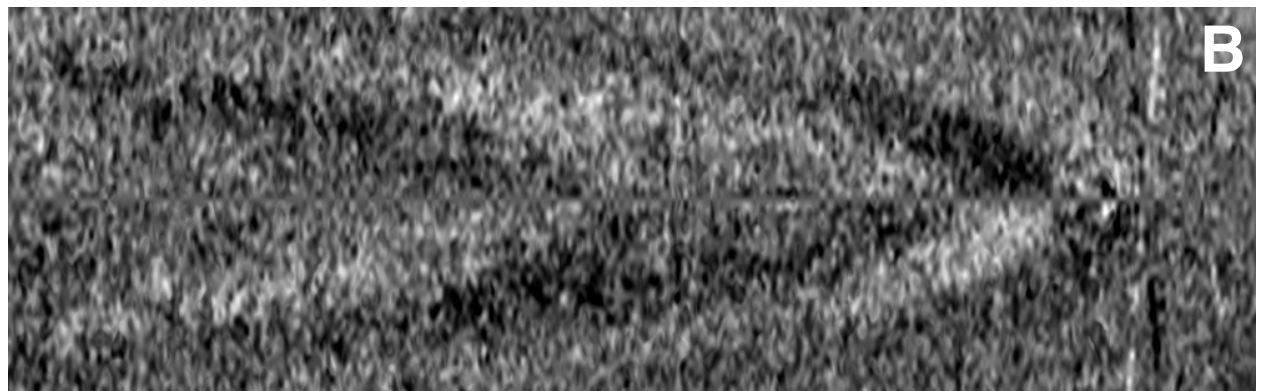
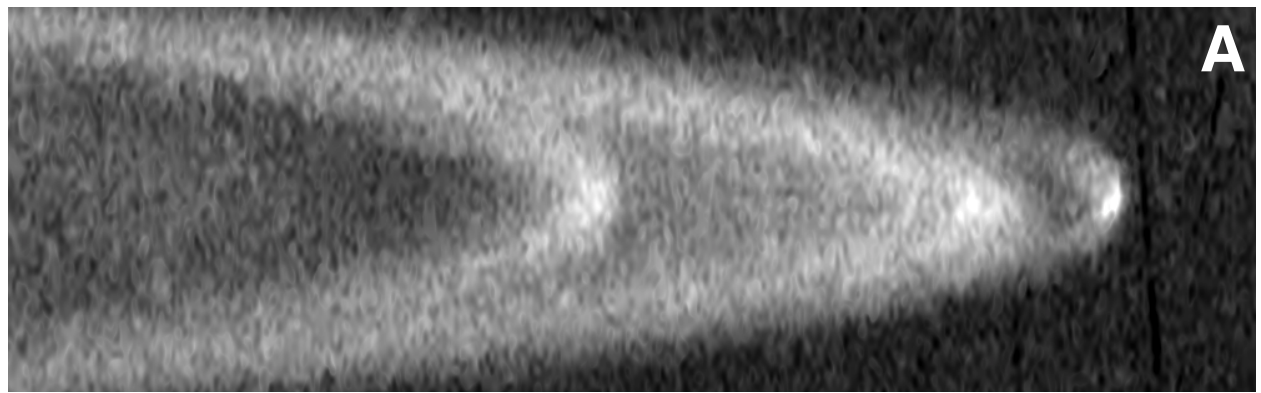
Materials, Methods and Models

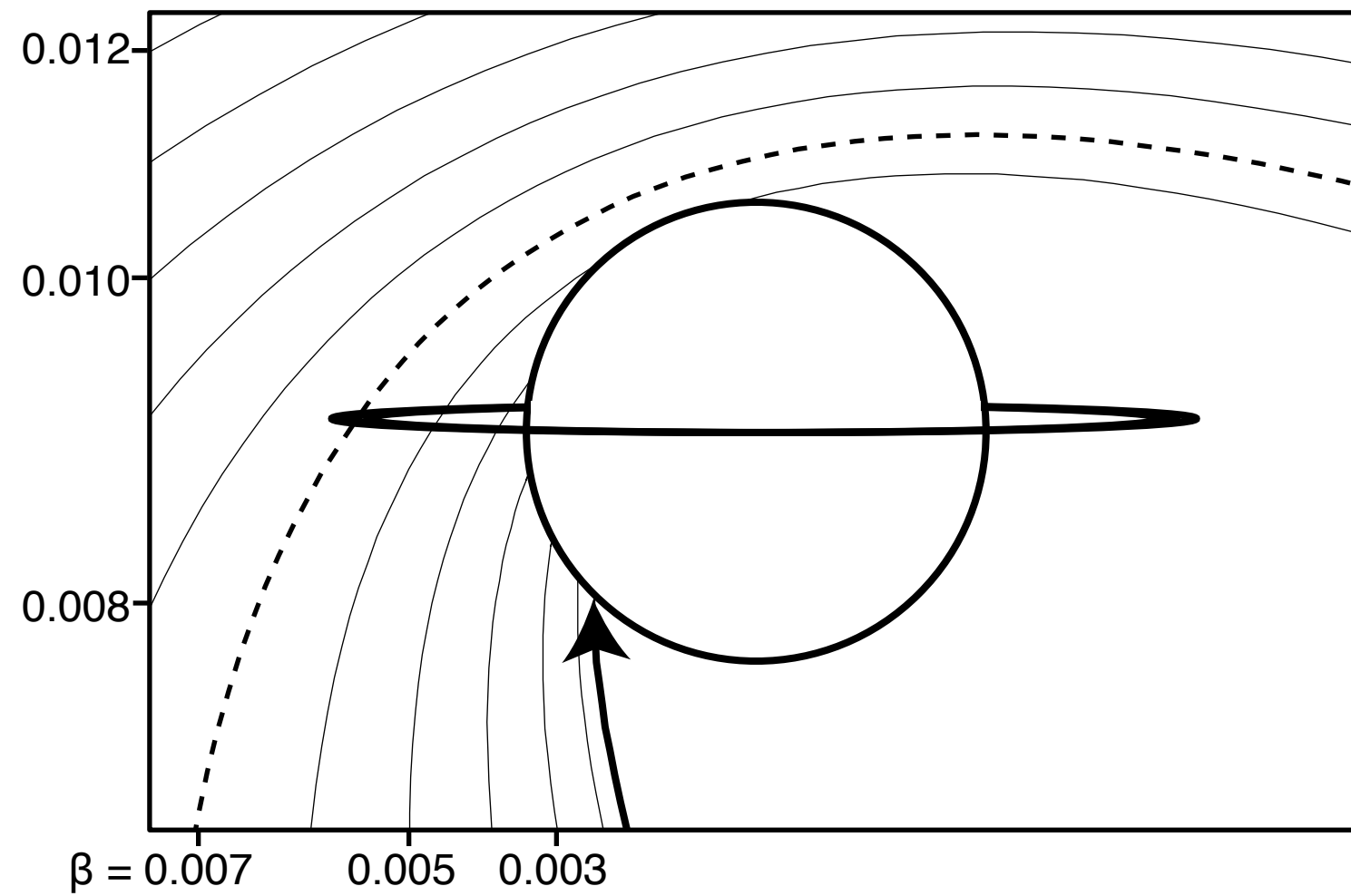
Figs. S1, S2, S3, S4, S5

Table S1











Supporting Online Material for

The Impact of Comet Shoemaker-Levy 9 Sends Ripples Through the Rings of Jupiter

M. R. Showalter, M. M. Hedman, and J. A. Showalter

correspondence to: mshowalter@seti.org

This PDF file includes:

Materials, Methods and Models
Figs. S1 to S5
Table S1

Materials, Methods and Models

1. Data Analysis

1.1 Ring Intensity Model

If a ring has spiral undulations of fixed wavelength λ and fixed amplitude Z_0 , then the vertical height of the ring surface can be defined by

$$Z(R, \theta) = Z_0 \sin(2\pi[R-R_0]/\lambda + [\theta - \theta_0]), \quad (\text{S1})$$

using polar coordinates (R, θ) , and with (R_0, θ_0) locating any zero point of the function. The radial and longitudinal components of the surface slope are, respectively,

$$\partial Z / \partial R = Z_0 \cos(2\pi[R-R_0]/\lambda + [\theta - \theta_0]) \cdot 2\pi/\lambda \quad (\text{S2})$$

and

$$1/R \partial Z / \partial \theta = Z_0 \cos(2\pi[R-R_0]/\lambda + [\theta - \theta_0]) / R, \quad (\text{S3})$$

The radial component is larger than the longitudinal by a factor $2\pi R/\lambda \ll 1$. This justifies our neglect of the longitudinal component; we treat the local slope as simply $Z' \equiv \partial Z / \partial R$.

We describe the observed intensity of the ring as a function $I(R, \theta)$. If the ring were flat and axisymmetric, then the intensity would be

$$I_{\text{flat}}(R) = I_{\perp}(R) / \sin(B), \quad (\text{S4})$$

where $I_{\perp}(R)$ is the intensity profile from a viewpoint perpendicular to the ring plane, and B is the ring opening angle, separating the line of sight from the equator plane. We define B to be nonnegative. The local slope of the ring changes the effective value of B . The unit surface normal vector at (R, θ) is

$$[-Z' \cos(\theta), -Z' \sin(\theta), 1] / (1 + Z'^2)^{1/2} \quad (\text{S5})$$

in rectangular coordinates $[x, y, z]$. If we define $\theta = 0$ along the ring radius vector perpendicular to the line of sight (Fig. 1A), then the unit vector pointing to the observer is

$$[0, -\cos(B), \sin(B)] \quad (\text{S6})$$

in the same coordinate frame. The complement of the angle between these vectors is the local, effective ring opening angle, B_{eff} . The inner product of Eqs. S5 and S6 determines this angle:

$$\sin(B_{\text{eff}}) = [\sin(B) + Z' \sin(\theta) \cos(B)] / (1 + Z'^2)^{1/2}. \quad (\text{S7})$$

In practice, B and Z' are both small, which leads directly to our model for intensity variations (Eq. 1):

$$I(R, \theta) = I_{\perp}(R) / \sin(B_{\text{eff}}) \approx I_{\text{flat}}(R) [1 - Z'(R, \theta) \sin(\theta) / \sin(B)]. \quad (\text{S8})$$

1.2 Image Processing

Table S1 lists the images used in this study. The Galileo images from 2000 provided our finest resolution on the Jovian ring, but required special handling to remove numerous bright spots caused by energetic particles hitting the CCD (Fig. S1). Each pixel was compared to the mean value of its four nearest neighbors, and if the difference exceeded a specified threshold, it was rejected. This process was repeated until it converged, and then the values of the rejected pixels were replaced by the local mean value.

The dark sky regions of the images are often nonzero, due to instrumental effects and to off-axis light entering the camera optics. In the Galileo images, the background light is generally rather uniform; it could be successfully modeled by a simple linear ramp function. New Horizons images were affected by a serious “ghosting” problem, however. We corrected this problem by noting that the pattern is nearly stable within the CCD, even though the rings are positioned at different locations. The rings occupy only a small portion of each image, so among the four images it became possible to map out the ghost pattern completely. This pattern was then subtracted from each of the images (Fig. S2).

We rotated each image into an orientation where the ansa line is exactly horizontal across the image. Images from the same set were adjusted and positioned to have identical geometry. This involved an iterative process using quantitative tests, such as maximizing the correlation or minimizing the root-mean-square (RMS) difference between pairs of images. We reprojected the images onto spatial grids roughly twice as fine as that of the sources; this ensured that the intrinsic spatial resolution of each image

was preserved. Within each set, the images were then co-added pixel by pixel to improve the signal-to-noise ratio. We rejected any pixels that were excessively bright in one image relative to the others, on the assumption that such pixels were probably corrupted. The combined images resulting from this processing were very clear and generally free of obvious flaws (Figs. 3A, S3).

1.3 Slope Derivation

A narrow strip of pixels centered on the ansa line of each image was resampled into a new rectangular grid in $(R, \sin(\theta))$ (Fig. S4A). To suppress noise, we employed a gaussian filter to blur the image by a few pixels prior to this step. Each column in the new image could then be described by a linear function $I = a + b \sin(\theta)$ (Eq. S8), where

$$I_{\text{flat}} = a \quad (\text{S9})$$

and

$$Z' = -b/a \sin(B) \quad (\text{S10})$$

(Fig. S4B,C; cf., 1C, 3C). We ignored the inner and outer regions of the resulting profiles $Z'(R)$, where values became highly erratic because I_{flat} was small.

1.4 Slope Modeling

For the Fourier analysis, we first trimmed away the innermost points in the slope profile, where no evidence for the ripple patterns could be seen; Figs. 1C, 3C and S4C show the ranges retained. The remaining data consists of a sequence of N radial locations R_k and slopes Z_k . Given wavelength λ , the Fourier amplitude is defined as $(A^2 + B^2)^{1/2}$, where

$$A = 1/N \sum Z_k \cos(2\pi R_k/\lambda) \quad (\text{S11})$$

and

$$B = 1/N \sum Z_k \sin(2\pi R_k/\lambda) . \quad (\text{S12})$$

Once we identified candidate wavelengths by their peaks in the Fourier analysis, we performed non-linear, least-squares fitting to the profiles to determine the optimal

wavelength, phase and amplitude of each sinusoidal pattern. Uncertainties correspond to $1-\sigma$ confidence intervals based on χ^2 statistics.

1.5 Chirp Modeling

Because of the nonlinear dependence of nodal regression rate on the radial distance from Jupiter, the numeric coefficient in Eq. 2 actually varies by $\sim 15\%$ between radial limits of 125,000 and 129,000 km in the Jovian system; see Hedman et al. (3) for formulas and details. As a result, the radial pattern is actually a “chirp”, not a sinusoid. Successive waves can be envisioned as changing linearly:

$$\lambda = \Lambda, \Lambda[1 + \varepsilon], \Lambda[1 + 2\varepsilon], \dots \Lambda[1 + N\varepsilon], \quad (\text{S13})$$

where Λ is the starting wavelength and $\varepsilon \ll 1$ describes the fractional change in wavelength from one cycle to the next. Successive cycles of this pattern will fall at radial locations:

$$R = 0, \Lambda, \Lambda[2 + \varepsilon], \Lambda[3 + 2\varepsilon], \dots \Lambda[N + \varepsilon(N^2 - N)/2]. \quad (\text{S14})$$

Converting the cycle number into a continuous variable x , we obtain

$$R(x) = \Lambda[x + \varepsilon x^2/2]. \quad (\text{S15})$$

However, we have chosen to model the ring patterns using a fixed wavelength λ instead:

$$R'(x) = R_0' + \lambda x. \quad (\text{S16})$$

How large are the errors that arise from this approximation? In least-squares fitting, the sinusoidal model will match the chirp as closely as is mathematically feasible, but features will necessarily shift. We estimate the magnitude of these shifts by defining $\Delta(x) \equiv R'(x) - R(x)$ and assuming that in the fitting procedure, the sinusoidal model will adjust to limit the extreme values of $|\Delta|$. Because $\Delta(x)$ is a parabola, this minimization is accomplished when

$$\Delta(0) = \Delta(N) = -\Delta(N/2). \quad (\text{S17})$$

These equations can be readily solved for the coefficients in Eq. S16, yielding

$$\lambda = \Lambda[1 + \varepsilon N/2]; \quad (\text{S18})$$

$$R_0' = \epsilon \Lambda N^2 / 16 \quad (\text{S19})$$

The second equation defines $\Delta_{\max} = \Delta(0)$, the upper limit on the radial offset arising from the assumption of a fixed wavelength. If we define $\Delta R = N\lambda$ as the full radial extent of our data, and $q = \epsilon N/2$ as the full fractional change in wavelength within this range, then

$$\Delta_{\max} = q/8 \Delta R . \quad (\text{S20})$$

Thus, although $q = 15\%$, the assumption of a fixed wavelength in our analysis introduces radial errors of only $\sim 2\%$ (80 km) in Figs. 1C and 3C. On the scale of these plots, such errors can be safely neglected.

Consistent with our intuition, a comparison of Eqs. S13 and S18 indicates that the best-fit fixed wavelength will be the value near the middle of the chirp. As a result, any determination of the elapsed time since a ripple pattern began must employ the winding rate relevant to the midpoint of the profile modeled.

2. Dynamical Models

2.1 Impact Dynamics and Tilt Amplitudes

We consider the consequences of a cometary dust grain impacting a ring particle. Working in the local frame of the ring before impact, momentum conservation can be stated

$$m_c \mathbf{v}_c = m_r' \mathbf{v}_r + m_e \mathbf{v}_e , \quad (\text{S21})$$

where m is particle mass, \mathbf{v} is velocity, and subscripts refer to the cometary impactor (c), the ring particle (r), and the impact ejecta (e). Boldface indicates a vector. For quantities that change during impact, final values are indicated by primes. Above, \mathbf{v}_e is understood to be the mass-weighted mean velocity of all ejecta after impact.

When $m_c/m_r > 10^{-7}$, a collision at tens of km/s is likely to result in catastrophic disruption (22), meaning that $m_r' \Rightarrow 0$. In this case, the initial momentum gets distributed over the total mass, and the resulting orbital tilt is

$$\begin{aligned} Z &= R v_{e\perp} / v_0 \approx R (v_{c\perp} / v_0) m_c / m_r \\ &= Z_{\max} m_c / m_r . \end{aligned} \quad (\text{S22})$$

Here, v_o is the orbital velocity of the ring particle, R is its orbital radius, and subscript \perp indicates the component of \mathbf{v} perpendicular to the ring plane. For convenience, we define $Z_{\max} = R (v_c/v_o)$, the tilt reached by a ring particle that intercepts its own mass. For the Jovian ring, $Z_{\max} \approx 130,000$ km.

Smaller impacts are non-disruptive cratering events, where yield factors are

$$Y \equiv m_e/m_c \sim 5 (v_c / [\text{km/s}])^2 \quad (\text{S23})$$

(23). In the Jovian ring, $v_c \sim 50$ km/s, implying $Y \sim 10^{-4}$. In this limit, the initial momentum is not distributed uniformly between the ring particle and the ejecta. Energy conservation can be written

$$\begin{aligned} f m_c v_c^2 &= m_r' v_r^2 + m_e [v_e^2 + \sigma^2(v_e)] \\ &= m_r' v_r^2 + m_e g v_e^2. \end{aligned} \quad (\text{S24})$$

Here f represents the fraction of the initial energy that goes into kinetic energy, rather than heat, after impact. Because v_e is the mean of a distribution, we must include $\sigma^2(v_e)$ to account for the difference between the square of the mean and the mean of the square. For convenience, we define $g = 1 + \sigma^2(v_e)/v_e^2$. Combining Eqs. S23 and S24 yields a momentum ratio

$$m_r' v_r / m_c v_c \sim (Yf/g)^{1/2}. \quad (\text{S25})$$

With f and g both expected to be of order unity and $Y \sim 10^4$, we conservatively predict this ratio to be ~ 30 . The reason the value is not unity is that the ejecta systematically carry momentum away from the impact site in the opposite direction. Compared to Eq. S22,

$$Z = R v_r/v_o = Z_{\max} m_c/m_r (Yf/g)^{1/2}. \quad (\text{S26})$$

This may appear to be gaining “something for nothing.” For an optically thick ring the ejecta would quickly deposit their opposite linear momentum elsewhere in the ring and the magnification factor would be lost. However, the Jovian ring’s optical depth $\tau \sim 10^{-5}$ (4,5) and collision time scales are measured in decades; the orbital nodes of the ejecta precess many times in the interim, preventing them from delivering any net tilt back to the ring.

Note that, because $m_c/m_r < 10^{-7}$ in Eq. S26, the largest possible tilt that can be imparted by a single, non-catastrophic collision is ~ 400 m; most deflections will be smaller. Therefore, to tilt the Jovian ring by ~ 2 km will require most particles to receive multiple impacts. Let $M(c)$ be the total integrated mass of comet particles of radius smaller than c , which pass through a ring of surface area A . The expected tilt reached by a ring particle of radius r is

$$Z(r) = Z_{\max} (Yf/g)^{1/2} \cdot M(r/K) / m_r \cdot \pi r^2 / A \quad (\text{S27})$$

This is Eq. S26 integrated over the cometary mass crossing the ring, and also scaled by the fractional cross-section of the ring particle. Here, $K \sim (10^7 \rho_c/\rho_r)^{1/3} \sim 200$ is the size ratio required for catastrophic collisions; we will show below that such impacts play a negligible role in the Jovian ring. We have assumed densities ρ_c and ρ_r are similar.

As a concrete application of Eq. S27, we define a nominal ring bounded by the orbits of Metis and Adrastea (128,000–129,000 km), yielding $A = 8 \times 10^8$ km². If this ring is composed primarily of bodies with $r = 1$ cm, then $M \sim 5 \times 10^{12}$ g of cometary dust must pass through it to achieve a 2-km tilt. This corresponds to a total volume of 0.005 km³, exclusive of grains larger than $r/K = 50$ μm.

2.2 Orbital Integrations

We carry out numerical integrations of the SL9 fragments' motion between their 1992 perijove and breakup through their July 1994 impacts. We employ a fourth-order Runge-Kutta integrator with adaptive step size. SPICE kernels obtained from the Planetary Data System (PDS) provide the positions of Jupiter, the Sun, the Galilean satellites, and Saturn, and a test particle responds accordingly. We include the J2 and J4 gravity moments of Jupiter, and allow for the effects of radiation pressure via a parameter β , which defines the ratio of the radiation pressure force to the Sun's gravity (15). By using the SPICE kernels, the problem is reduced to one of integrating individual test particles rather than integrating the entire Solar System. Other perturbations on the comet, such as those caused by outgassing and erosion, are neglected. Lorentz forces are completely negligible for particles in the size range we consider.

The SPICE kernels provide the initial position and velocity for 21 fragments of SL9 at the time of their 1992 perijove. However, the values are not sufficiently precise to integrate the fragments' motion over long periods of time. To compensate, we begin by tabulating the position of each fragment at one-day intervals from perijove to impact, using SPICE tools. We then solve for the initial state vector that minimizes the RMS residuals between the integrated and tabulated locations. Upon completion of this procedure, our integrator matches the motion of each fragment with residuals of a few hundred km. This discrepancy is small compared to the spread among the fragments' trajectories; we therefore regard our integrations as representative of SL9, even if they differ slightly from the best orbital models (11).

We then explore the perturbations needed for a particle to hit the ring instead of the planet. Typical ejection speeds of dust grains from the fragments are ~ 1 m/s (14). Neglecting radiation pressure, our integrations show that such speeds are insufficient to bypass the planet; relative speeds of ~ 30 m/s are required before the paths of ejecta can intersect the ring.

Figure 4 shows sample integrations in which solar radiation pressure has been included. Shown are the paths of dust grains through the system in 1994, after having been launched with zero initial velocity from fragment K at its 1992 perijove. In the limit of geometric optics, particle size and β are inversely related (15):

$$\beta(c) \approx 0.33 \text{ } \mu\text{m}/c . \quad (\text{S28})$$

The coefficient is uncertain, depending on the albedo and density of the cometary grains, but the inverse relationship holds regardless. We adopt this relationship in the discussion to follow, while noting that uncertainty in the absolute scaling remains.

Figure 4 can be summarized by a function $\mathbf{R}(c)$, defining the ring plane intercept point for a comet particle of size c , if launched from a fragment at the time of the 1992 perijove. A more complete description of the impactors must also include their dependence on the moment t at which they are launched; this could occur at any time between the perijove and the impact ~ 742 days later. The resulting function $\mathbf{R}(c, t)$ is nearly independent of the source fragment, so we use K for all further analysis. Our integrations also reveal that small (~ 1 m/s) random velocities at the time of ejection do not change the results significantly.

Because our integrations are deterministic, for any given launch time t there exists a range of particle sizes (c_1, c_2) that will later intersect the nominal ring (Fig. S5); these are the solutions to the equations $|\mathbf{R}|(c_1, t) = 129,000$ km and $|\mathbf{R}|(c_2, t) = 128,000$ km. The mean follows a roughly linear decrease from $c_0 \approx 50 \mu\text{m}$ at perijove to near zero just before impact. The fractional width $\Delta c/c = 0.5\text{--}0.7\%$ over this time span. At any given moment, only ejecta within a very narrow range of sizes will be launched onto paths that later intersect the ring, but *every* particle in this size range will do so. This is an idealized view of the system, surely, and neglects a variety of randomizing effects such as the slightly different trajectory of each fragment, the effects of rotation and vaporization, and the small ejection velocity of each grain. Such factors will “blur out” the narrow size distribution of ring impactors at any given moment. Nevertheless, the distribution of impactors launched at time t will still be centered on roughly the same size and will still carry a comparable fluence of mass into the ring.

2.3 Impactor Populations and Dust Fluence Estimates

We distinguish two populations of particles that serve as potential impactors into the Jovian ring. First are those grains created during the breakup event around perijove in 1992. The existence of this population (P1) is supported by early images of SL9, in which the fragments are already shrouded by a broad stream of dust (16). A second population (P2) comprises those particles that were ejected after breakup (14).

Colliding populations typically obey a power-law model, in which

$$n(c) dc = n_j (c/\mu\text{m})^{-p} dc \quad (\text{S29})$$

defines the total number of particles in the size range c to $c+dc$. The coefficient n_j has dimensions of length $^{-1}$, making the integral over c dimensionless. We apply the subscript $j = 1$ or 2 to distinguish models for populations P1 and P2, respectively. Exponent p is typically 2–4, which ensures that the mass of the population is dominated by the upper end of the distribution,

$$M_j(c_{\max}) = 4\pi/3 \rho_c n_j (c_{\max}/\mu\text{m})^{4-p} / (4-p) \mu\text{m}^4, \quad (\text{S30})$$

where c_{\max} is the upper cutoff. For $p = 4$, both limits come into play, but the dependence is only logarithmic:

$$M_j(c_{\min}, c_{\max}) = 4\pi/3 \rho_c n_j \log(c_{\max}/c_{\min}) \mu\text{m}^4. \quad (\text{S31})$$

Population 1 was created within a short time span around perijove at $t = 0$. As the integrations illustrate, only particles in a narrow size range will intersect the ring. Total mass within this range can be expressed as a fraction of the mass in P1. It is convenient to divide P1 into the particles smaller and larger than c_o , because only the former can possibly interact with the ring. Referring exclusively to the smaller particles, the fractional mass F_1 intersecting the ring is $(\Delta c/c_o) (4-p)$ or, if $p = 4$, $(\Delta c/c_o) \log(c_{\min}/c_0)$. In either case, the coefficient on $(\Delta c_o/c_o)$ is of order unity, yielding $F_1 \sim 0.5\%$.

Population 2 was created continuously during SL9's final orbit. In this case, the information in Fig. S5 enables us to determine the fraction F_2 of particles smaller than c_o that intersect the ring. If the dust is ejected at a uniform rate, then the fraction of particles of size c intersecting the ring is simply $F_2(c) = [t_2(c) - t_1(c)]/P$, where $P \approx 742$ days is the orbital period and (t_1, t_2) are the solutions to $|\mathbf{R}|(c, t_1) = 129,000$ km and $|\mathbf{R}|(c, t_2) = 128,000$ km. We can integrate $F_2(c)$ times the size distribution to determine the total mass fraction F_2 of particles smaller than $c_o = 50 \mu\text{m}$ that intersect the ring. We find a roughly linear trend with p , with $F_2 = 0.35\%$ for $p = 2$ and $F_2 = 0.15\%$ for $p = 4$. The fractions F_1 and F_2 are similar, permitting us to adopt 0.2–0.5% as the fraction of SL9 dust that will intercept our nominal 1000-km wide ring.

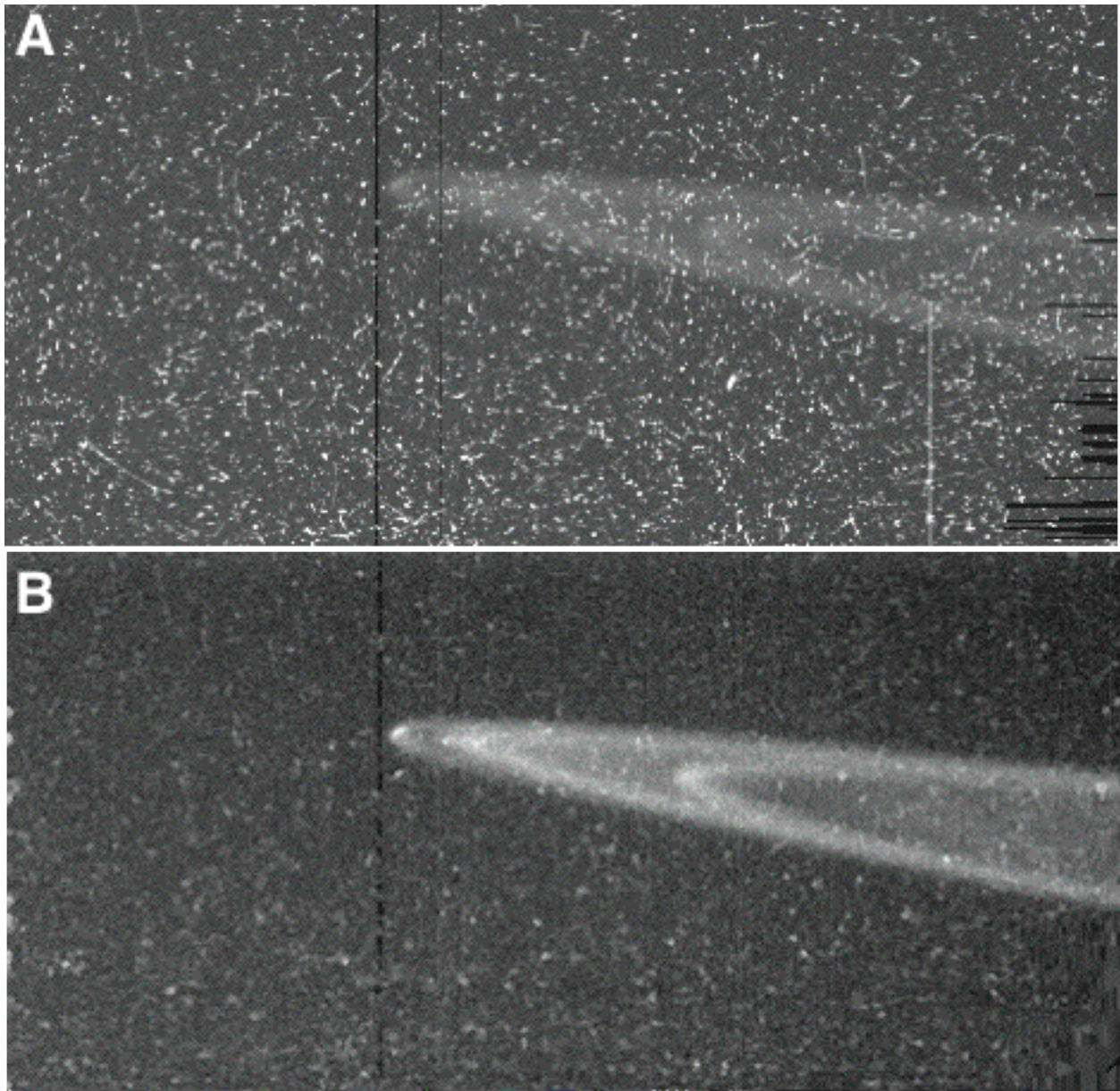


Fig. S1.

(A) Charged particles hitting the CCD created a dense overlay of corrupted pixels in Galileo image C0552599400. (B) An iterative procedure systematically masked out any pixels that were too different from their nearest neighbors. The resulting image is much cleaner. Combined analysis of this image with C0552603500, taken 39 minutes later, produced the image shown in Fig. 3A.

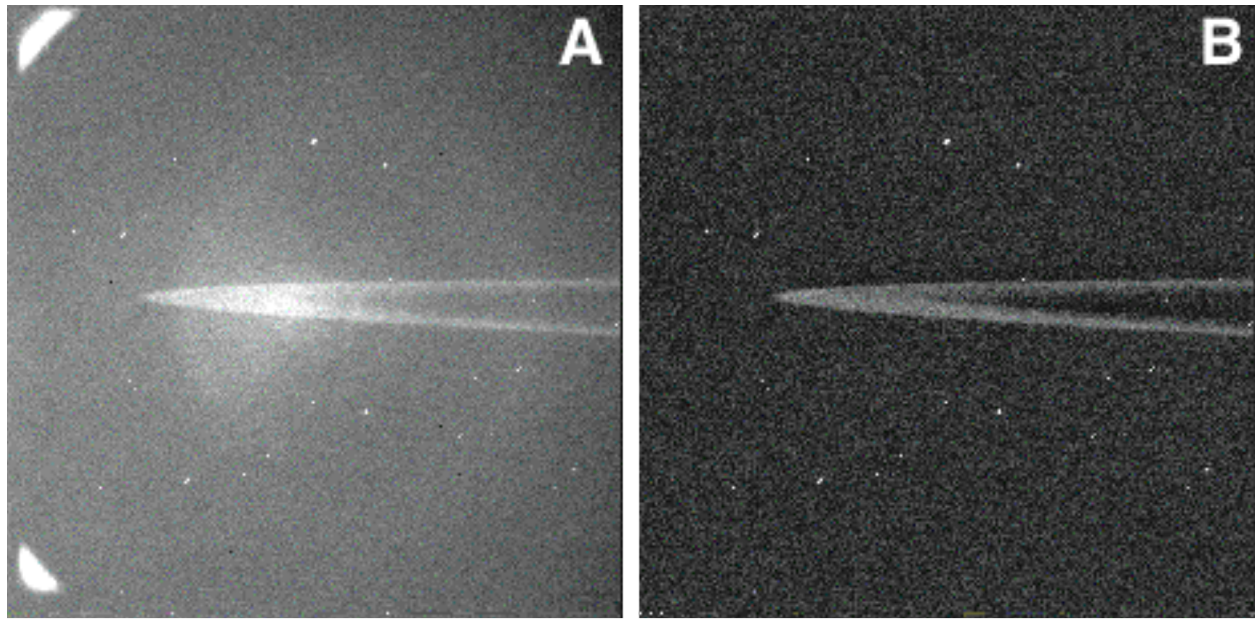


Fig. S2.

“Before” and “after” versions of New Horizons image 0035079924. (A) The image initially showed a “ghost” pattern from light scattered within the optics. However, three other images showed a similar pattern but with the ring falling at slightly different positions within the frame. This made it possible to isolate the ghost pattern and subtract it away from each image (B).

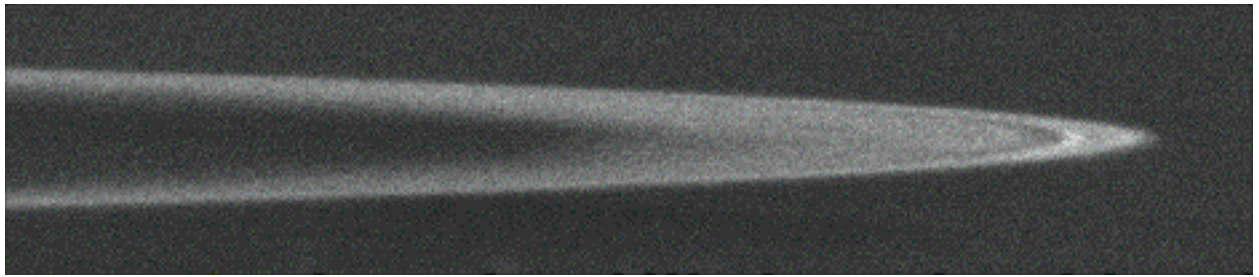


Fig. S3.

The final, rotated and co-added version of our four New Horizons images.

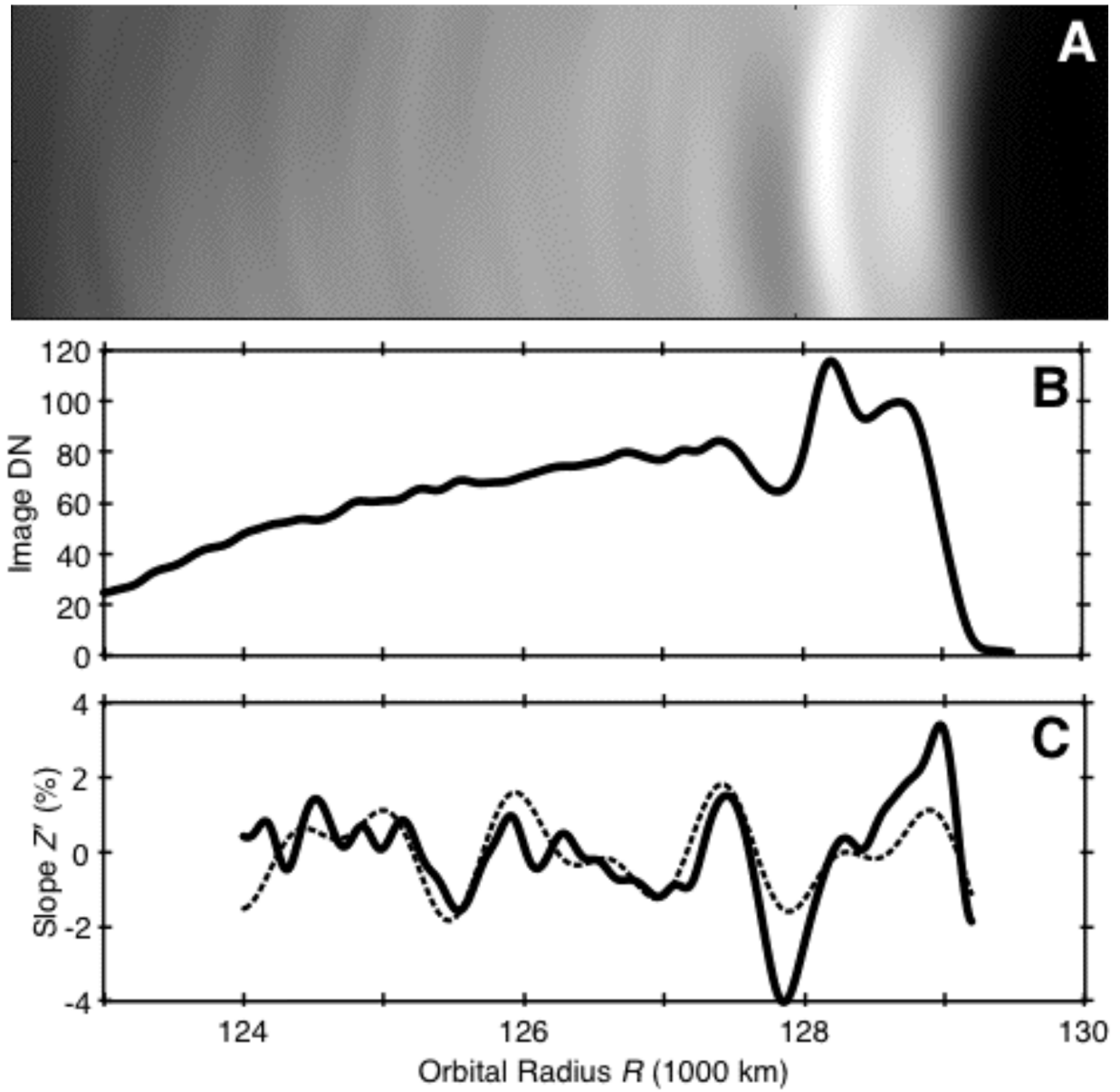


Fig. S4.

(A) The ring tip in Fig. S3 has been reprojected onto a uniform grid in $[R, \sin(\theta)]$. The columns of this image can then be modeled as described in the text to produce (B), a mean radial profile of ring intensity, I_{flat} , and (C), a model for the ring slope. The dashed line shows a best-fit model comprising two sinusoids: $\lambda_1 = 1315$ km; $Z_1 = 2.3$ km; $\lambda_2 = 775$ km; $Z_2 = 1.0$ km. The third peak in the Fourier transform, which we associate with SL9 in Fig. 2C, has a much smaller amplitude and is not included in this model.

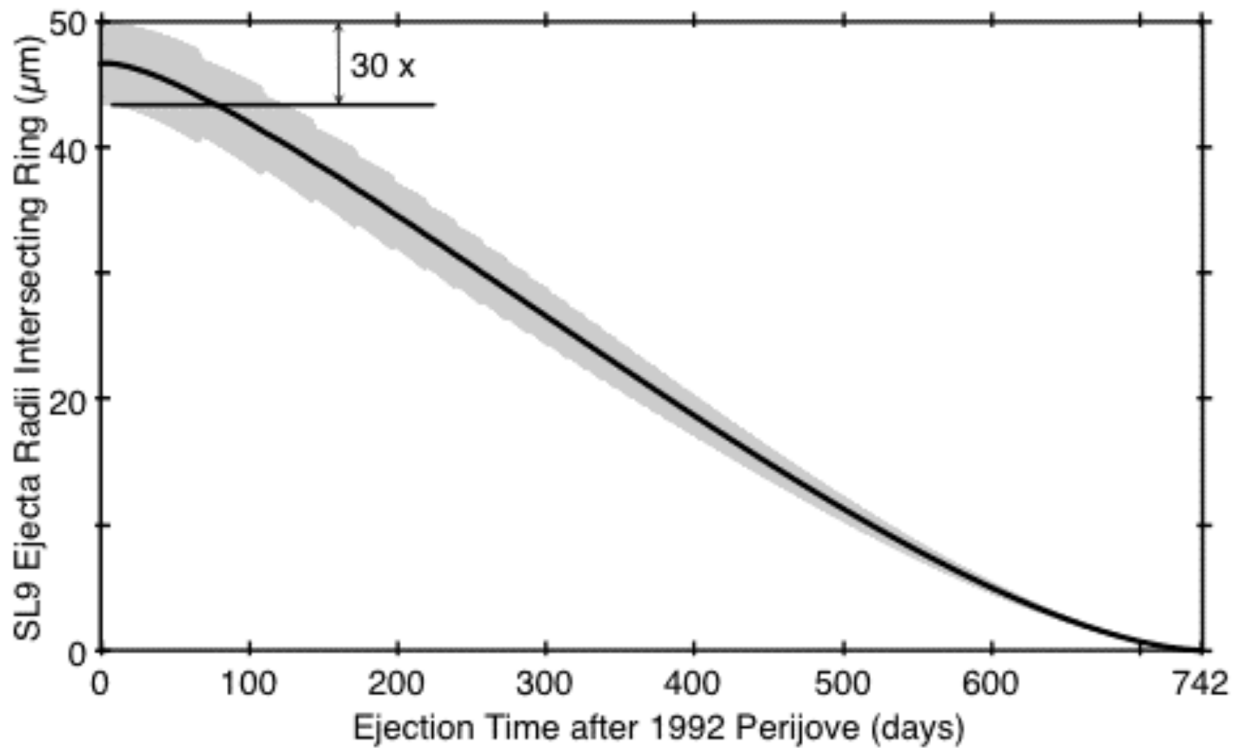


Fig. S5.

The size of a cometary dusty grain destined to impact the Jovian ring, based on the date of release at low velocity from fragment K. The gray zone represents the size range around the mean that will intersect a 1000-km wide ring. This zone has been expanded by a factor of 30 to make it more visible in the figure; typically, the vertical width is 0.5–0.7% of the mean.

Table S1.

Summary of images.

Image Set	Image ID	Observation Time	Opening Angle B (°)	Range to Jupiter (1000 km)	Image Resolution (km/pixel)	Phase Angle (°)
Galileo 1996						
	C0368974139	1996-11-09T04:15	0.48	2,259	22	179.2
	C0368991900	1996-11-09T07:15	0.48	2,333	23	178.3
	C0368992339	1996-11-09T07:20	0.48	2,331	23	177.6
Galileo 2000						
	C0552599400	2000-05-21T12:30	0.45	639	6.4	21
	C0552603500	2000-05-21T13:11	0.39	663	6.6	5.8
New Horizons 2007						
	0035079784	2007-03-01T18:31	0.79	3,488	17	139
	0035079854	2007-03-01T18:32	0.79	3,489	17	139
	0035079924	2007-03-01T18:33	0.79	3,490	17	139
	0035080321	2007-03-01T18:40	0.79	3,496	17	139